PUBLICATIONS OF THE ASTRONOMICAL SOCIETY OF THE PACIFIC, **124**:1318–1335, 2012 December
© 2012. The Astronomical Society of the Pacific. All rights reserved. Printed in U.S.A.

MMT and Magellan Infrared Spectrograph

BRIAN MCLEOD, DANIEL FABRICANT, GEORGE NYSTROM, KEN MCCRACKEN, STEPHEN AMATO, HENRY BERGNER, WARREN BROWN, MICHAEL BURKE, IGOR CHILINGARIAN, MAUREEN CONROY, DYLAN CURLEY, GABOR FURESZ, JOHN GEARY, EDWARD HERTZ, JUSTIN HOLWELL, ANNE MATTHEWS, TIM NORTON, SANG PARK, JOHN ROLL, AND JOSEPH ZAJAC

Harvard-Smithsonian Center for Astrophysics, 60 Garden Street, Cambridge, MA 02138

HARLAND EPPS

UCO/Lick Observatory, University of California, Santa Cruz, CA 95064

AND

PAUL MARTINI

Department of Astronomy, The Ohio State University, Columbus, OH 43210

Received 2012 October 09; accepted 2012 November 07; published 2012 December 4

ABSTRACT. The MMT and Magellan infrared spectrograph (MMIRS) is a cryogenic multiple-slit spectrograph operating in the wavelength range 0.9–2.4 μm. The refractive optics of MMIRS offer a $6'.9 \times 6'.9$ field of view for imaging with a spatial resolution of 0.2 arcsec pixel^{-1} on a HAWAII-2 array. For spectroscopy, MMIRS can be used with long slits up to 6′.9 long, or with custom slit masks having slitlets distributed over a $4' \times 6'.9$ area. A range of dispersers offer spectral resolutions of 800–3000. MMIRS is designed to be used at the f/5 foci of the MMT or Magellan Clay 6.5 m telescopes. MMIRS was commissioned in 2009 at the MMT and has been in routine operation at the Magellan Clay Telescope since 2010. MMIRS is being used for a wide range of scientific investigations from exoplanet atmospheres to Lyα emitters.

1. INTRODUCTION

MMIRS (McLeod et al. 2004) is a cryogenic imaging spectrograph that can be used at the f/5 foci of the converted MMT or the Magellan Clay telescopes. MMIRS operates in the wavelength range 0.9–2.4 μm and performs spectroscopy with slit masks or long slits. Commissioned in 2009 at the MMT and Magellan, MMIRS has been in routine operation at the Magellan Clay telescope since 2010 (see Fig. 1). The MMIRS design is based on the FLAMINGOS (Florida Multiobject Imaging Near-IR Grism Observational Spectrometer) and FLAMINGOS2 instrument concepts (Elston 1998, 2003; Eikenberry et al. 2006) developed at the University of Florida, but MMIRS was independently engineered from the ground up by our group.

A new generation of infrared multiple-object spectrographs is becoming available at a number of 6.5 to 10 m telescopes. In addition to MMIRS, these instruments include the Multi-Object Infrared Camera and Spectrograph (MOIRCS) at Subaru (Suzuki et al. 2008), LBT Near Infrared Spectroscopic Utility with Camera and Integral Field Unit for Extragalactic Research (LUCIFER) at the Large Binocular Telescope (LBT) (Seifert et al. 2010), Multiobject Spectrometer for Infrared Exploration (MOSFIRE) at Keck (McLean et al. 2012), and soon FLAMINGOS 2 at Gemini (Eikenberry et al. 2006) and EMIR (Espectrógrafo Multiobjeto Infrarojo) at Gran Telescopio Canarias (Garzon et al. 2006). MOIRCS was ready for scientific operations in 2006, followed by LUCIFER and MMIRS in 2009, and MOSFIRE in 2012. The interest in this new generation of spectrographs is based on our conviction that infrared imaging and spectroscopy are poised to answer a number of high-impact questions in astronomy, from the formation of the first galaxies and the star formation history of the universe, to the formation of stars in our own Galaxy.

One of our major goals for MMIRS is developing a physical understanding of high-redshift galaxies. For example, galaxy metallicities are estimated from the strong nebular emission lines Hα, [NII], [OIII], Hβ, and [OII]. These rest-frame optical emission lines are redshifted in the near infrared for high-redshift galaxies, and can be efficiently observed in the redshift ranges: $0.75 < z < 1.05$ (Hα in J band), $1.28 < z < 1.74$ (Hα in H band, [OIII] in J-band), and $2.0 < z < 2.7$ (Hα in K band, [OIII] in H band, [OII] in J band). Well-documented techniques (e.g., Kewley & Dopita 2002; Kewley et al. 2004) allow us to determine gas-phase abundances with [OIII], [OII], and Balmer emission lines. The metallicity evolution of high-redshift galaxies places an important constraint on their star formation history, and relates to mass loss and changing gas fractions in the galaxies. To a limit of $K = 20.1$ ($K_{AB} = 22$) the surface density of galaxies in the $1 < z < 2.7$ range is roughly 3.5 arcmin^{-2} so

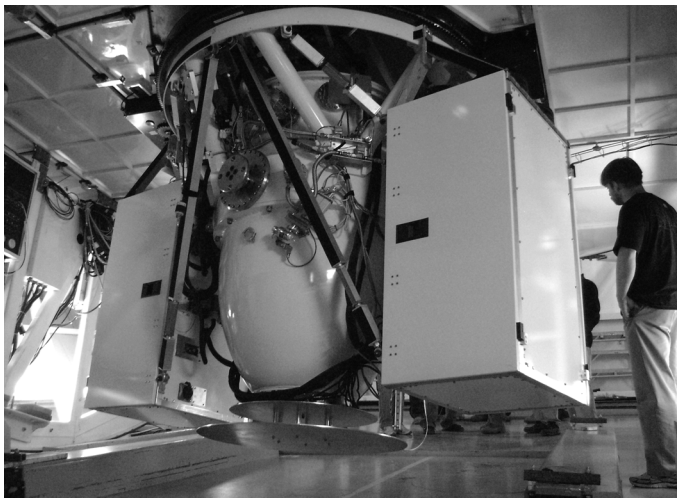

FIG. 1.—MMIRS at the MMT in 2009.

that the surface density of high-redshift galaxies is well matched to the multislit capability and sensitivity of MMIRS.

MMIRS's broad scientific appeal is demonstrated by the diverse range of observations undertaken in the past two years. In the nearby universe, MMIRS has been used for studies including transiting exoplanet atmospheres (Bean et al. 2011), dust chemistry in post-AGB stars (Hart et al. 2011), a planetary nebula in the Sagittarius Dwarf (Otsuka et al. 2011) and the nature of X-rays sources in the Galactic center (Servillat et al. 2011). At cosmological distances, MMIRS has been used to study Lyα emitters (Hashimoto et al. 2012), the physical properties of $z \sim 1.5$ galaxies, and high-redshift lensed galaxies.

We describe MMIRS's optics in § 2, its mechanical and thermal design in § 3 and 4, and its electrical design in § 5. In § 6 we describe the major challenges that we had to overcome to bring MMIRS into operation. In § 7 we describe MMIRS's software and in § 9 and 10 daytime operations and observing protocols. We conclude in § 10 with a description of MMIRS's scientific performance. We use Vega-referenced magnitudes throughout unless explicitly noted.

2. OPTICAL DESIGN

2.1. Overview

The MMIRS optical train consists of a vacuum-spaced doublet field corrector, a six-element corrector, and a six-element camera. The 520 mm focal length collimator operates at f/5.2, producing a 100 mm diameter collimated beam. The 285 mm focal length camera operates at f/2.85 and produces a focal plane scale of $0.''201$ pixel^{-1} for the 18 μm detector pixels. The field of view subtended by the 2048×2048 pixel HgCdTe Astronomical Wide Array Infrared Imager-2 (HAWAII-2) detector is $6'.9 \times 6'.9$. The field corrector produces sharp images across the extended $14'$ diameter field of view used for guiding.

The optical layout is shown in Figure 2. The optical design uses five materials: CaF_2, BaF_2, ZnSe, Infrasil, and the Ohara optical glass S-FTM16 (Brown et al. 2004). During the optical design process several constraints were introduced into the optimization operands to control ghost images. Ghost analysis shows that there are no significant ghost images or ghost pupils in the MMIRS optics, other than low-level reflections from the back of slit masks and the filters. The optics, including AR coatings, were fabricated by Janos Technologies.

The final as-built prescription is given in Table 1. The monochromatic rms image diameters (including alignment errors not shown in Table 1) averaged over wavelengths between 0.9 and 2.45 μm are 11 μm and 16 μm at the field center and corners, respectively. The worst monochromatic rms image diameter is 30 μm at any field angle or wavelength. The monochromatic 90% encircled energy diameters averaged over wavelengths between 0.9 and 2.45 μm are 18 μm and 23 μm at the field center and corners, respectively. The worst monochromatic 90% image diameter is 42 μm at any field angle or wavelength. The design has a maximum lateral color of 19 μm across the full wavelength range at full field, or 12 μm across any of the standard photometric bands. The final scale is $0''.2$ per 18 μm pixel. After our design was complete, improved cryogenic refractive index measurements by the Cryogenic High Accuracy Refraction Measuring System (CHARMS) group at Goddard Space Flight Center (Leviton et al. 2005; Leviton et al. 2007) became

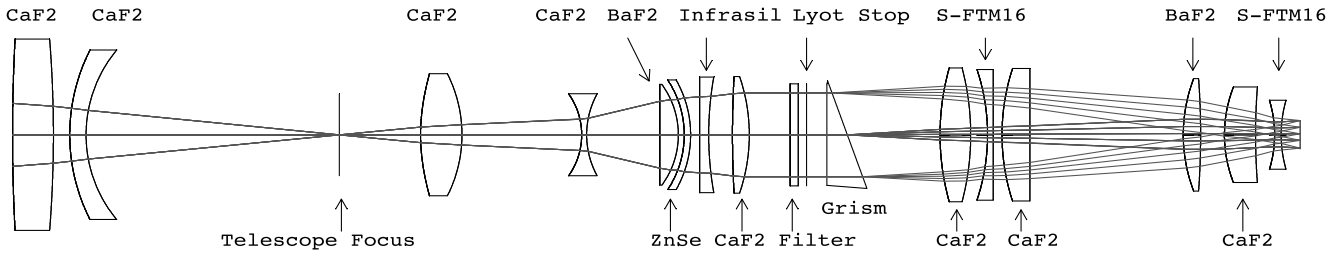

FIG. 2.—MMIRS optics configured in spectroscopic mode. For imaging, the disperser following the Lyot stop is removed. The overall distance from the telescope focus to the detector (on the far right) is 1.18 m. The optics include 8 CaF_2, 2 BaF_2, 2 S-FTM16, 1 INFRASIL, and 1 ZnSe lenses. All lenses are singlets that are antireflection coated on both sides. The collimator operates at f/5.2 and the camera at f/2.8.

TABLE 1
AS-BUILT OPTICAL PRESCRIPTION

Surface	Surface Type	Radius	Thickness	Glass	Diameter	Conic	Comment
OBJ	STANDARD	Infinity	Infinity	AIR_10C_554T	0	0	
STO	STANDARD	−16255.3	0	MIRROR	6502.4	−1	
2	STANDARD	Infinity	−6179.235	AIR_10C_554T	—	0	
3	STANDARD	−5150.890	0	MIRROR	1592.584	−2.6947	
4	STANDARD	Infinity	6179.235	AIR_10C_554T	—	0	
5	STANDARD	Infinity	1430.149	AIR_10C_554T	—	0	
6	STANDARD	2209.039	50.040	CAF2_10C_ABS	234.15	0	Lens 1 Corrector
7	STANDARD	−1492.450	20.000		234.15	0	
8	STANDARD	229.065	20.090	CAF2_4C_ABS	207.35	0	Lens 2 Corrector
9	STANDARD	162.343	310.000		207.35	0	
10	STANDARD	Infinity	99.398		—	0	Focus
11	EVENASPH[a]	235.280	50.659	CAF2_76K_CHARMS	149.31	0	Lens 1 Collimator
12	STANDARD	−165.238	146.536		149.31	0	
13	STANDARD	−86.493	6.092	CAF2_76K_CHARMS	100.33	0	Lens 2 Collimator
14	STANDARD	104.594	89.332		100.33	0	
15	STANDARD	Infinity	22.872	BAF_76K_CHARMS	123.20	0	Lens 3 Collimator
16	STANDARD	−104.278	7.234		123.20	0	
17	STANDARD	−121.250	7.816	ZNSE_76K_CHARMS	134.12	0	Lens 4 Collimator
18	STANDARD	−135.736	11.041		134.12	0	
19	STANDARD	Infinity	11.069	I301_76K_CHARMS	141.54	0	Lens 5 Collimator
20	STANDARD	406.740	29.090		141.54	0	
21	STANDARD	1291.376	20.586	CAF2_76K_CHARMS	142.72	0	Lens 6 Collimator
22	STANDARD	−220.874	50.000		142.72	0	
23	STANDARD	Infinity	10.000	I301_76K_CHARMS	125.00	0	Filter
24	STANDARD	Infinity	10.000		—	0	
25	STANDARD	Infinity	163.500		100.00	0	Lyot Stop
26	STANDARD	304.883	37.478	CAF2_76K_CHARMS	163.59	0	Lens 1 Camera
27	STANDARD	−325.003	20.653		163.59	0	
28	STANDARD	−253.737	6.979	S-FTM16_L10_76	159.85	0	Lens 2 Camera
29	STANDARD	Infinity	10.739		159.85	0	
30	STANDARD	262.371	34.005	CAF2_76K_CHARMS	162.18	0	Lens 3 Camera
31	STANDARD	Infinity	187.848		162.18	0	
32	STANDARD	192.373	21.201	BAF2_76K_CHARMS	137.44	0	Lens 4 Camera
33	STANDARD	−966.735	29.159		137.44	0	
34	STANDARD	160.885	38.080	CAF2_76K_CHARMS	116.85	0	Lens 5 Camera
35	STANDARD	757.961	23.302		116.85	0	
36	STANDARD	−144.813	8.071	S-FTM16_L14_76	84.47	0	Lens 6 Camera
37	STANDARD	154.348	23.172		84.47	0	
IMA	STANDARD	Infinity			52.13	0	Detector

[a] Aspheric coefficients: $a_4 = -5.2750111 \times 10^{-8}$, $a_6 = 2.1900236 \times 10^{-12}$, $a_8 = -7.7923832 \times 10^{-17}$.

available. We found that a refocus restored the original image quality when the CHARMS indices were adopted. Cold tests of the optics with test masks confirm that we achieve the expected performance.

2.2. Field Corrector

A doublet CaF_2 field corrector lies in front of the f/5 Cassegrain focus of the converted 6.5 m MMT or Clay Magellan Telescope and produces f/5.2 images with an rms spot diameter less than 0″.1 over a 14′ field of view. The design of Cassegrain field correctors is discussed by, e.g., Su et al. (1990), Wilson (1996), Epps and Fabricant (1997).

The first element of the MMIRS corrector also serves as the vacuum window of the cryostat. The 50 mm thickness of this element limits its internal stress to 125 psi under atmospheric pressure. The second corrector element is inside the cryostat, but cools only slightly by radiation to the cold mechanisms below. The second element serves as a radiation shield for the first element, keeping the first element close to the ambient temperature and preventing condensation from forming.

2.3. Collimator and Lyot Stop

The 520 mm focal length collimator has six elements, three made of CaF_2, and one each of BaF_2, ZnSe, and Infrasil. At f/5.2, the collimator produces a 100 mm diameter collimated beam with a pupil 65 mm from the back vertex of the final collimator lens. The pupil blur over the full range of field angles and wavelengths is ± 2.5 mm. The physical Lyot stop is placed just beyond the optimal pupil position due to physical constraints.

The leading surface of the first collimator lens is aspheric with fourth-, sixth- and eighth-order terms and a maximum aspheric departure of 0.19 mm. This surface was diamond-turned, post-polished, and tested with subaperture stitching interferometry.

The Lyot stop was laser cut from 0.2 mm thick anodized aluminum foil by PhotoMachining of Pelham, NH. The 33 mm diameter central obscuration in the stop is supported by 0.75 mm wide spider arms. These were made as thin as possible to minimize the amount of blocked light. Because the Lyot stop does not rotate, the spider will not in general line up with the telescope spider as the telescope tracks.

2.4. Filters and Dispersers

The 125 mm diameter, 10 mm thick filters are located just before the Lyot stop. We currently have seven broadband filters: Y, J, H, K_s, $K_{\rm spec}$, zJ, and HK. The first four are the standard imaging and spectroscopic filters, augmented by the latter three for spectroscopy. Table 2 summarizes the filter characteristics and vendors.

The disperser wheel follows the Lyot stop. We currently have three surface-relief grisms: J, H, and HK, all obtained from the Richardson Grating Laboratory. H and K volume phase holographic gratings (produced by Kaiser Electro-Optics) with beam straightening prisms (produced by ISP Optics) will be installed in 2013. Table 3 lists the disperser details. The available spectroscopic observing modes are summarized in Table 4.

TABLE 2
FILTERS

Band	50% Transmission limits	Peak transmission	Vendor
zJ	0.949–1.500	0.94	Materion-Barr
Y	0.966–1.072	0.94	Research Electro-Optics
J	1.172–1.330	0.92	Research Electro-Optics
H	1.498–1.786	0.96	Research Electro-Optics
HK	1.253–2.489	0.92	Omega Optical
K_s	1.996–2.318	0.86	Research Electro-Optics
$K_{\rm spec}$	1.931–2.451	0.98	Omega Optical

TABLE 3
DISPERSERS

Band	Lines mm^{-1}	Prism angle in	Prism angle out	Prism material
J (ruled)	210	0°	20.1°	Infrasil
H (ruled)	150	9.2°	26.7°	Infrasil
HK (ruled)	81.6	9.2°	26.7°	Infrasil
H (VPH)	290	9.5°	9.5°	ZnSe[a]
K (VPH)	200	8.8°	8.8°	ZnSe[a]

[a] VPH gratings use a pair of identical prisms.

2.5. Camera

The 280 mm focal length camera was based on an earlier design for FLAMINGOS-2 (Epps & Elston 2003). The f/2.8 camera contains six elements, three made of CaF_2, two of S-FTM16, and one of BaF_2. The first infrared camera design using S-FTM16 known to the authors was a five-element system developed by Stephen Shectman in 1999 (private communication).

2.6. Guider and Wavefront Sensing Optics

An annular tent mirror directs light outside the science field (to a maximum radius of 7′) to two opposing guider/wavefront sensor assemblies. The light reflected from the tent mirror passes through two opposing vacuum windows, and the guiders are located outside the dewar. The tent mirror was diamond-turned from a single piece of stress-relieved aluminum 6061 and post-polished.

The guider optics are designed to work from 6000 Å to 9000 Å because MMIRS is primarily a bright-time instrument. Each guider assembly is mounted on a three-axis stage (x, y, and focus). The focal plane is relayed 1:1 onto the guide cameras using a symmetric pair of custom achromatic lenses. The field of view of each guide camera is $1'.3 \times 1'.3$.

In normal operation, one camera is used for guiding, and the other operates as a wavefront sensor, feeding images to the observatory active optics system (Schechter et al. 2003;

TABLE 4
SPECTROSCOPIC MODES

Wavelength range	Disperser	Order	Filter	Pixels/ spectrum	Resolution
0.96–1.07	HK	2	Y	360	1600
0.96–1.07	J	1	Y	520	2400
0.96–1.07	H	2	Y	670	3000
0.95–1.50	HK	$1+2$	zJ	var	800,1600
0.94–1.51	J	1	zJ	2600	2400
1.17–1.33	J	1	J	720	2800
1.25–2.45	HK	1	HK	1800	1400
1.50–1.79	H	1	H	800	2400
1.50–1.79	H (VPH)	1	H		3000
1.98–2.32	HK	1	K	550	1700
1.95–2.45	K (VPH)	1	$K_{\rm spec}$		3000

Pickering et al. 2004). To use the guider as a Shack–Hartmann wavefront sensor, a stage containing two fold mirrors and the wavefront sensor optics is moved into the beam. The first fold directs the light through a 4″ field stop that reduces sky background. The beam is then folded through a second collimator that forms an 8 mm diameter pupil image on an Adaptive Optics Associates lenslet array with a 0.6 mm pitch and 40 mm focal length. A final fold mirror directs the image to the CCD camera. No refocus is required when switching between guiding and wavefront sensing. A 20 μm pinhole illuminated by an LED is used to calibrate the Shack–Hartmann spot positions. The pinhole assembly is attached to the guider baffle inside the cryostat and the guider assembly is translated in front of the illuminated pinhole for calibration. Stars brighter than $R = 16$ allow guiding with 1 s cadence, and stars brighter than $R = 14.5$ allow wavefront sensing with 30 s integrations.

2.7. Calibration Optics

The calibration system is housed in a compact system that mounts directly above the main instrument. The light source is a LabSphere 250 mm integrating sphere with a Spectralon coating. The 50 mm exit port of the sphere is conjugated to the Lyot stop using a Fresnel Technologies POLY-IR5 IR-transmissive Fresnel lens. The system illuminates the full $7' \times 7'$ field with an f/5 beam. Two 25 mm ports on the sphere contain continuum lamps and an Ar Penray line lamp. During calibration a polished aluminum fold mirror translates into the beam to send light to the instrument below.

3. MECHANICAL AND THERMAL DESIGN

3.1. Mechanical and Thermal Overview

Figure 3 is an external view of MMIRS. The total instrument mass is ∼2 metric tons. The slit mask chamber shown in Figure 4 is a vacuum vessel at the top of the instrument sealed at the top by the first corrector lens and at the bottom by a gate valve. The slit mask chamber and all of its contents can be disconnected from the bulkhead that forms the top of the main instrument chamber. The slit mask chamber contains the corrector optics, the Dekker wheel for aperture selection, the slit mask wheel, a dewar assembly, and the guider pick off mirror. The gate valve, located between the slit mask wheel and the first collimator lens, isolates the optics and detector during slit mask exchange. The gate valve is mounted to the top bulkhead of the main instrument chamber.

The toroidal slit mask LN_2 reservoir is supported by an insulating G-10 ring from the bottom flange of the slit mask chamber. The top of the slit mask LN_2 reservoir serves as the mounting plate for the slit and Dekker wheels and the guider pick off mirrors. To the sides are two windows that pass the guider light outside the cryostat. The cold baffle that blocks thermal emission from the warm gate valve is mounted to the central wall of the slit mask chamber LN_2 reservoir.

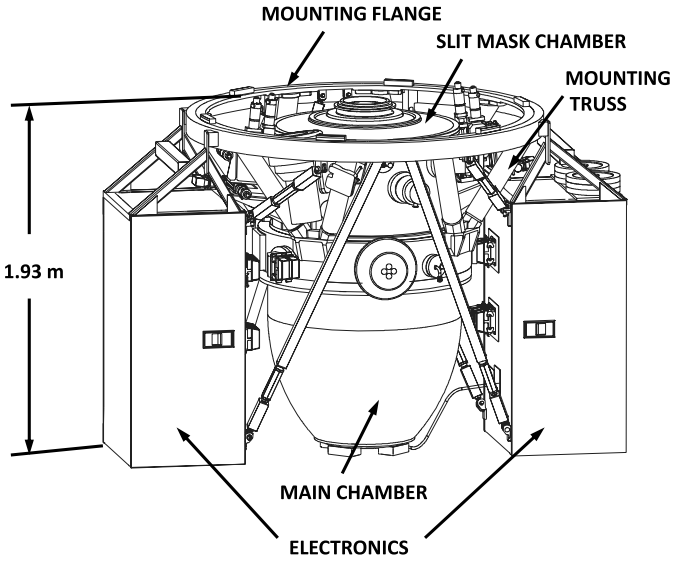

FIG. 3.—Exterior view of MMIRS. The overall height of the instrument is 1.93 m, and the distance from the top of the corrector to the detector is 1.6 m. The two electronics racks are mounted directly to the mounting flange.

The main chamber (Fig. 5), sealed at the top by the gate valve, contains the collimator optics, Lyot stop, filter and disperser wheels, camera optics, and detector assembly. A second G-10 ring mounted on the inside of the main chamber bulkhead supports the D-shaped LN_2 reservoir in the camera section. The face of this reservoir is the main optical bench supporting the collimator and camera optics, disperser and filter wheels, and the detector assembly. All major aluminum cryogenic

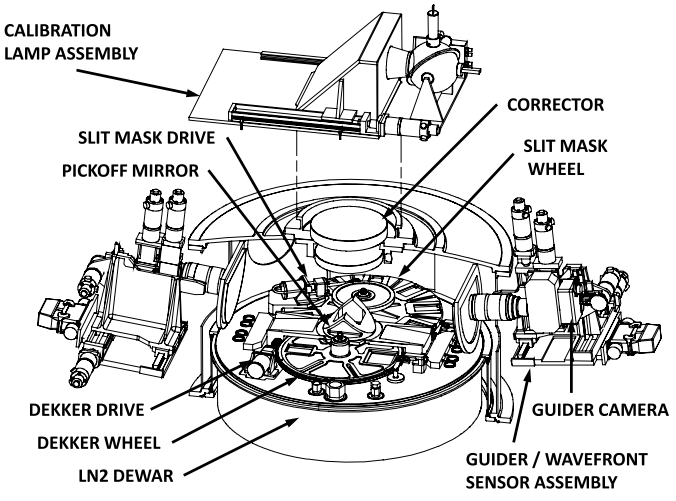

FIG. 4.—Layout of the slit chamber. The calibration lamp assembly is shown in the calibration position; during observation the fold mirror assembly is retracted to the left. Two identical guiders view through windows on opposite sides of the instrument. This chamber can be thermally cycled during the daytime to allow mask exchange.

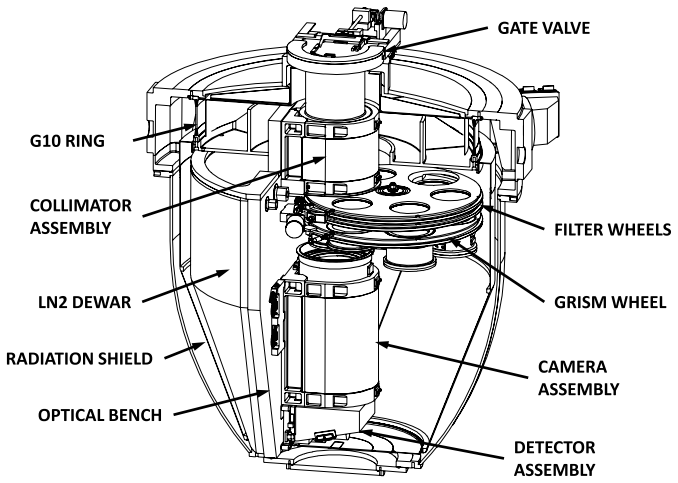

FIG. 5.—Layout of the main chamber. The main chamber contains the collimator, camera, dispersers and filter. The main chamber is isolated from the slit chamber by a gate valve when masks are exchanged.

components in MMIRS were stress relieved by cooling from room temperature to 77 K at several steps during the machining process.

MMIRS contains ten mechanisms: a calibration fold mirror slide, two guider assemblies, a Dekker wheel, a slit mask wheel, a gate valve (and its baffle), two filter wheels, a disperser wheel, and a detector focus assembly. The basic characteristics of these mechanisms are summarized in Table 5. All of the internal mechanisms are driven by 200 step revolution^{-1} Phytron VSS-52 vacuum rated stepper motors with 0.35 N-m of holding torque. The external guider mechanisms are driven by normal duty Phytron ZSS-52 stepper motors with 0.45 N-m of torque.

Effective thermal design of MMIRS requires balancing competing factors: (1) to minimize dark current the detector should be as cold as possible, (2) to avoid damage the optics and detector cannot be cooled or warmed too rapidly, (3) the slit masks need to be warmed and cooled as rapidly as possible to allow convenient daytime exchange, and (4) the system should be as simple as possible. Our approach was to build MMIRS around two liquid nitrogen dewars which are coupled as tightly as possible to the spectrograph components. We control the detector and optics warmup and cool down rates by regulating heater power or the flow of LN_2. To validate this approach we constructed a detailed thermal finite element model of MMIRS to verify cool down and LN_2 consumption rates.

Radiation shields surround the cold spectrograph components. The radiation shields are 1.26 mm thick aluminum 1100 sheet metal supported with G-10 standoffs for thermal isolation from the warm and cold surfaces. A single layer of aluminized Mylar covers both sides of the G-10 rings, the radiation shields, and much of the LN_2 tank surfaces. Electrical connections pass though connectors mounted on the thermal shield flange. The flange connectors allow easy shield removal and provide a light-tight shield penetration. Multiple sensors in each chamber provide temperature information.

3.2. Guider Assembly

The two guider translation axes and the wavefront sensor translation axis are linear stages mounted on THK rails and driven by ballscrews. Stepper motors drive the ballscrews through 6.25:1 planetary gearheads, providing a 4.8 μm stepsize. The guider focus mechanism uses similar rails, encoders, and gearboxes, but is cam-driven over a 2 mm range with 1.8 μm resolution.

The guider CCD cameras are based on Steward Observatory and Carnegie Observatory designs. The guider electronics are adapted from a Carnegie Observatory design, repackaged to allow the CCD head to be separated from the readout electronics. The readout electronics use five printed circuit boards (power, clocks, signal processing, timing generator, and amplifiers), interfaced to a small backplane. We house this system in an aluminum box measuring $160 \times 95 \times 85$ mm. Input of control signals and output of video data is via a fiber optic link to an interface card on the PCI bus of the host computer. Internal

TABLE 5
MECHANISMS

Mechanism	Mechanism type	Gearing	Position sensing
Calibration mirror	Ballscrew linear	Planetary	Hall effect limits/home
Guiders	3 ballscrew linear (positioning)	Planetary	Hall effect limits/home Magnetic tape encoder
	1 cam-driven linear (focus)	Planetary	Magnetic tape encoder
Dekker wheel	Rotary with sapphire thrust bearing	Worm gear at outer radius	Microswitch detent detection/home
Slit mask wheel	As Dekker	Worm gear at 40% radius	As Dekker
Gate valve	Ballscrew linear	90° worm gear	Microswitch/reed switch limits/home
Disperser wheel	As Dekker	As Dekker	As Dekker
Filter wheels	As Dekker		As Dekker
Focus stage	Cam driven linear	Pinion/spur	LVDT

voltages derive from a single 48V DC power input, and total power dissipation for the system is approximately 12 W (excluding thermoelectric cooling).

We use an E2V CCD47-20 CCD, a thinned backside-illuminated frame-transfer device with 1024×1024 active pixels (13 μm square). The CCD is housed in a vacuum-tight aluminum box measuring approximately $120 \times 85 \times 45$ mm (not including the small vacuum valve, electrical connector, and heat extractor). Internal cooling of the CCD to -20°C or lower is provided by a three-stage Melcor thermoelectric cooler, with the heat being transferred through the back of the housing to a small fan-cooled heat sink. Maximum power for the TE cooler is 12 W.

The remote CCD head connects to the readout electronics box via a multicoax cable. To better buffer the CCD output signals for remote operation, small preamplifiers have been added inside the head for the two video channels. Tests have shown no performance degradation with cable lengths of up to 6 feet.

3.3. Slit Mask and Dekker Wheels

The Dekker wheel is used to limit the field of view for spectroscopy (see Fig. 6). The wheel carries five apertures: one for long slits, one for short slits, one for slit masks, a blocking mask, and an open aperture for imaging. A stepper motor drives a Vespel (polyimide) worm which engages a gear machined into the outer edge of the wheel. Wheel positions are selected with mechanical detents (also at the wheel edge) that are sensed with a microswitch. There is enough backlash in the drive gear to allow the detent to seat fully and control the wheel positions. An extra detent position located near the open aperture detent provides a unique sequence of detents for home sensing at power up. A sapphire ball thrust bearing creates a thermally conductive path from the wheel to the liquid nitrogen dewar. The Dekker wheel and slit mask wheel are primarily cooled through a Vel-therm conductive path at the rotary shaft as discussed in § 6.1.

The slit wheel mechanism is similar to the Dekker wheel, but it contains a square imaging aperture, seven long slits varying in size from 0″.2 (1 pixel) to 2″.4 (12 pixels), and nine multislit masks, each $4' \times 7'$. The slit wheel is driven through a gear having 40% of the diameter of the wheel to avoid interfering with the exchange of the slit masks. A port on the vacuum vessel allows radial insertion/withdrawal of the slit mask holders for mask exchange.

3.4. Slit Mask Dewar

The liquid nitrogen dewar has fill and vent lines arranged to limit LN_2 loss at extreme telescope orientations. The full slit mask dewar volume is 55 liter, but the fill is limited to 45 liter by the fill and vent port locations, yielding a hold time of 40 hr.

The stiffened front surface of the slit mask dewar is the mounting surface for the Dekker wheel, the slit mask wheel and the guider pick off mirror. A G-10 tube assembly structurally connects the dewar to the vacuum vessel. The G-10 tube is epoxied into aluminum mounting rings using Stycast 2850-FT epoxy with a 0.25 mm bond thickness. The G-10 tube minimizes the conductive heat loss from the dewar and provides compliance to accommodate the thermal contraction of the dewar.

3.5. Gate Valve

The gate valve is a slightly customized version of a VAT Inc. catalog item. The 40 mm thick gate valve is thin enough to fit in the 100 mm gap between the slit and the first collimator lens.

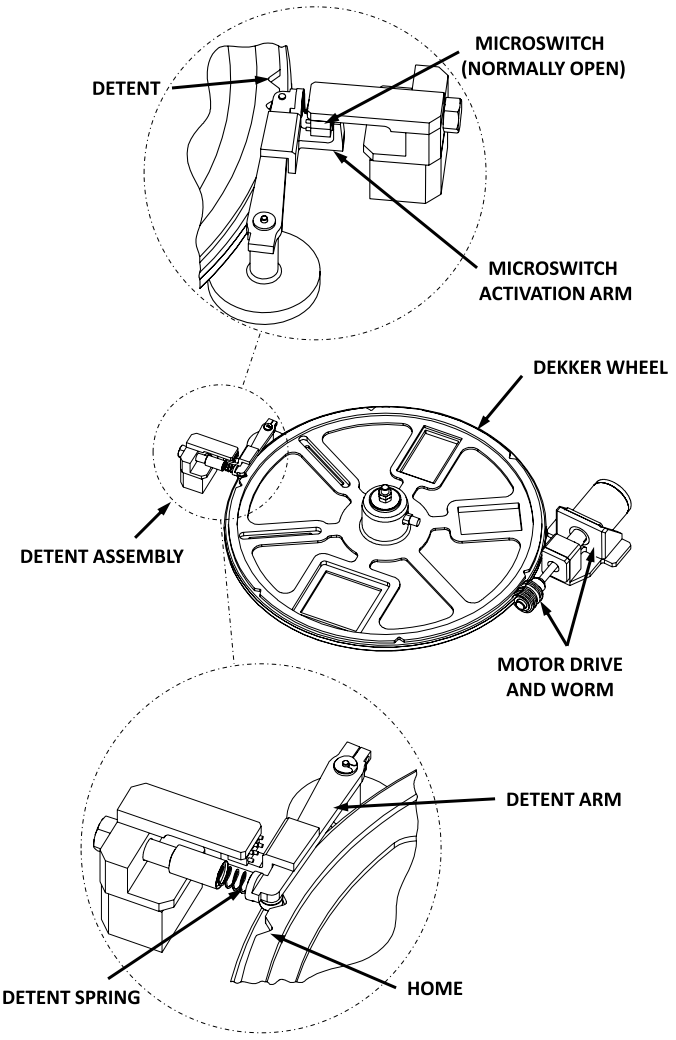

FIG. 6.—Drive and detent mechanisms for the Dekker wheel. A stepper motor drives the wheel through a worm gear. An arm on the detent assembly depresses a microswitch to sense detent positions. The slit mask, filter, and disperser wheels operate in the same fashion.

The VAT valve components are combined with a custom stepper motor driven ballscrew assembly. The stepper motor drives the ballscrew through a worm gear. Microswitches sense the closed and open positions.

3.6. Disperser and Filter Wheels

Both six-position filter wheels carry five filters with one open aperture. The disperser wheel is a six-position wheel intended to carry five dispersers with one permanent open aperture. The drive and detent scheme for the filter and disperser wheels is very similar to the Dekker wheel described previously. No Vel-therm supplemental conductive path was required in the disperser and filter wheels because they are cooled quite slowly to avoid stressing the optics. The disperser wheel is balanced with counterweights to minimize the required drive torque.

3.7. Focus Stage

The detector focus mechanism is a linear stage with a cam drive shown in Figure 7. The cam is stepper motor driven through a gear reduction. The stage slides on sapphire balls in machined raceways that are spring loaded together. The stage is spring loaded against a cam drive that provides a 5 μm motion per motor step with a range of ± 2.5 mm. An LVDT provides position readout with 1 μm resolution. The stage is cooled primarily via 0.25 mm-thick copper foil straps that connect the detector housing to the fixed portion of the stage. In practice, the focus stage is rarely moved, as the spectrograph is quite stable over extended time periods.

3.8. Main Dewar and Optical Bench

The optical bench/dewar assembly is used to cool and support the components in the main chamber. The assembly is composed of four main structural elements: (1) The front bulkhead is a deep section forging that provides the mounting interface to the telescope truss. The gate valve separating the slit mask chamber from the main chamber is mounted on this bulkhead. LN_2 and electrical feedthroughs penetrate the bulkhead. (2) A G-10 ring assembly with aluminum end fittings supports and thermally isolates the cold components. It is similar to the G-10 ring in the slit mask chamber. (3) A deep section support ring connects the G-10 ring to the optical-bench/LN_2 dewar assembly. (4) The optical-bench/LN_2 dewar consists of a 50 mm thick lightweight top plate welded to a curved bottom section. Three internal stiffening ribs welded to the underside of the top plate provide stiffness and thermal contact to the LN_2.

The LN_2 reservoir has a total capacity of 80 liter, limited to 60 liter by the fill and vent locations and yielding a 56 hr hold time when MMIRS is zenith pointing. The hold time is comfortably greater than 24 hr in normal operation.

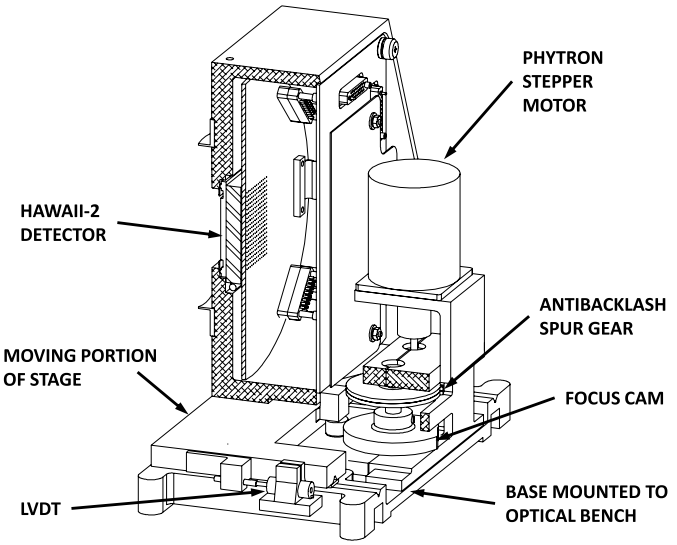

FIG. 7.—Detector assembly with focus stage. The HAWAII-2 array detects light incident from the left. For focus, a stepper motor positions a linear stage by rotating a cam through reduction gears.

3.9. Flexure Performance

The flexure between the slit and the detector is ≤ 1 pixel, measured between zenith angle 0° and 45°, at all rotation angles. During the course of a typical 2 hr observation block we see less than 0.2 pixels flexure. Our design goal was less stringent: <1 pixel in any 2 hr observation period. The differential flexure between the guider and the slit was measured in the lab to be approximately 1 pixel between 0° and 60° zenith angle. We are able to observe up to 2 hr following mask alignment with a misalignment of less than 25% of the slit width. Under these conditions slit losses due to misalignment are typically less than 10%.

3.10. Vacuum System

MMIRS has a built-in turbo pump system used to evacuate the slit mask chamber and the main chamber. The entire instrument can be pumped to a pressure of 10^{-4} torr in less than 4 hr. Each chamber has a cold charcoal adsorption cartridge conductively coupled to the LN_2 dewar for pumping nitrogen and other noble gases when the cryostat is cold and the turbo pump system disconnected. The vacuum pump system consists of a Varian Triscroll 600 pump and V-301 turbo pump mounted to the slit mask chamber. The main chamber is evacuated through the gate valve. Vacuum gauges are mounted on right angle elbows to minimize illumination of the optics. Redundant gauges and solenoid valves are provided to control the backfill process for slit mask exchange and other operations. This backfill system is controlled by a safety interlock system to avoid instrument damage (see § 5.3).

4. OPTICS MOUNTS

4.1. Design Goals

The design goal was to limit internal stress under any operating condition to less than 400 psi for the crystalline materials (CaF_2, BaF_2, and ZnSe) elements, and less than 500 psi for the S-FTM16 and Infrasil elements. The maximum anticipated stresses are during shipping and cool down or warmup. We adopted a 10 g maximum shipping load and a maximum 0.15 K min^{-1} temperature change during cool down and warmup.

4.2. Spring-loaded Mount Design

The MMIRS cryogenic optics mount design (Fig. 8) uses aspects of the optics mounts used in the Gemini Near Infrared Spectrograph (GNIRS) (Elias 2006) and the Gran Telescopio Canarias EMIR (Barrera et al. 2004). The lenses are mounted in aluminum housings. Radially, they are constrained by two Delrin pads 40° in angular extent to maintain acceptable lens stresses during shipping and cool-down/warmup. The thickness of the pads is chosen so that the lenses are centered at room temperature and also at 77 K. All the Delrin parts were made from the same batch of material, of which we had the CTE measured. The radial spring forces are provided by compression springs selected from the Lee Spring catalog.

Axially each lens is constrained by three raised aluminum pads each 40° long and 5 mm wide. A 75 μm thick Kapton spacer is placed between the pad and lens. The opposite side of the lens provides the axial spring force via a Teflon spacer, an aluminum spacer with three more matching raised pads, a custom made beryllium copper Belleville spring and an aluminum spring retainer. The springs were designed to provide a 10 g preload.

Figure 9 shows the complete camera assembly with light shield and mounting arrangement. The camera barrel assembled from the individual lens mounts is clamped to a V-block base that is in turn bolted to the optical bench. The collimator optics are assembled in a similar fashion.

4.3. Alignment of Lens Assemblies

Our tolerance analysis indicated that we can tolerate radial positioning errors of each lens distributed uniformly within a 75 μm radius circle. The tilt error tolerance was <0.1 mrad for the alignment of each lens's optical axis relative to its optical flats, and the same tolerance for the bezel axial flats relative to the assembly's optical axis. No axial, radial, or tilt adjustments were provided so our approach was to measure the lens positions as described below and to correct manufacturing errors where possible. Although we did not meet the tolerances above, ray tracing indicated that our basic goal of a <12 μm rms image diameter contribution from assembly errors was met.

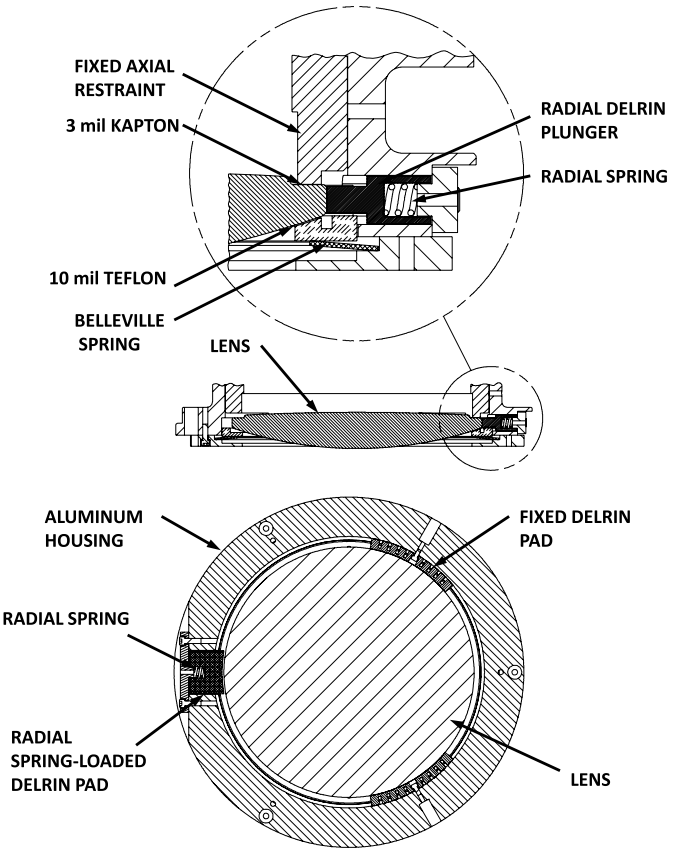

FIG. 8.—Layout of a typical lens mount showing the radial and axial supports.

The process of verifying that the parts were made correctly or correcting machining errors, developing the procedure to safely insert each lens into its housing, and verifying that each lens ended up in the correct place required approximately one week per lens. Critical dimensions of each part were measured (with digital calipers or with a coordinate measuring machine) and then the parts were cleaned and inspected for burrs under a microscope.

After each lens was installed we measured its decenter, tilt, and axial placement relative to its housing using a TriOptics Opticentric machine. The Opticentric consists of a rotary table on an air bearing. The table has tip-tilt and X-Y translation manual control. Located on either side of the table is an autocollimator equipped with a video camera. Using an appropriate head lens on each autocollimator focused at the center of curvature of the lens surface we see the autocollimator cross hairs in focus on the camera. We then adjust the tilt and translation of the table to bring the lens optical axis onto the rotary axis of the air bearing. The final step is to measure the mechanical runout of the lens housing using a digital indicator. We can also measure the axial position of the lens by focusing the autocollimator head lens onto the surface of the lens under alignment. Our measurement repeatability with the Opticentric is less than 10 μm of

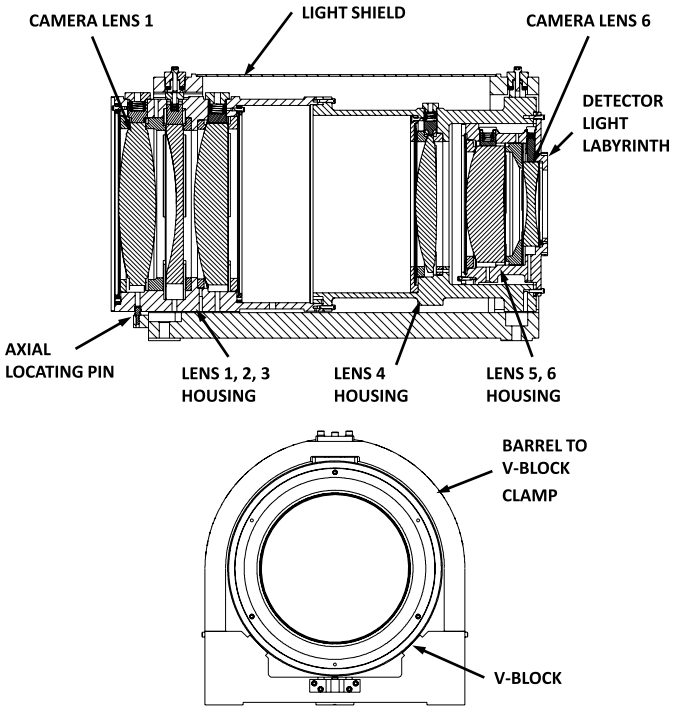

FIG. 9.—Camera assembly showing the overall mounting scheme for the six camera lenses.

decenter, 0.1 mrad of tilt, and 25 μm axially. Our measurements show that we achieved a mean radial centration error of 45 μm and a maximum error of 90 μm. We achieved a mean tilt error of 0.22 mrad and a maximum tilt error of 0.75 mrad.

5. ELECTRICAL DESIGN

5.1. Electrical Overview

The MMIRS electrical system is housed in two instrument mounted racks containing all control electronics for the system. Rack 1 contains all motion control and calibration system control components and provides the interface to facility power and network connectivity. Rack 2 houses temperature and vacuum control, and the science detector interface. Temperature control of the detector is provided by a Lakeshore 321 controller, and cryostat temperatures are monitored using two Lakeshore model 218 monitors. Chamber warm-up and cool-down control, as well as gate valve temperature control is provided by four Omega Ethernet temperature controllers. Three Pfeiffer vacuum gauges are controlled by a Pfeiffer controller. Vacuum pump control is provided by means of switched power to an externally mounted scroll pump and a rack mounted Varian V301-AG turbo pump controller. Each rack contains a guider power supply and electronics box and an Acromag six-channel temperature monitor used to track rack internal temperatures. Both racks are insulated and include a heat exchanger and fan connected to the facility liquid cooling loop. A thermostat in each rack cuts off AC power should the cooling system fail. The total power dissipation in the two racks is 700 W.

5.2. Motion Control

The motion control system is a compact PCI-bus version of the Delta-Tau UMAC system. All of the motion axes are driven by Phytron stepper motors and drivers. The Phytron PAB93-70 drivers are mounted in three 4U 19 inch rack mount boxes. The Phytron driver provides for intelligent setup and control of motor run parameters and readout of motor temperature, bus voltage and current. The setup of the drives is provided by a serial interface on each Phytron driver, which in turn connects to a serial to Ethernet converter. The Delta-TAU system provides real-time motor direction and control.

5.3. Vacuum and Interlock System

A vacuum interlock system implemented in hardware monitors the pressure and temperature on both sides of the gate valve. The interlock system prevents the gate valve from being opened when the two chambers are at different temperatures or pressures. It also locks out the back fill valves so the slit mask chamber cannot be raised to ambient pressure if (1) the gate valve is open and either optics section is cold or if (2) the gate valve is closed and the slit chamber is cold. Finally, the interlock prevents the slit chamber heaters from being turned on when the gate valve is open.

5.4. Detector Electronics

The camera controller and data acquisition interface are the same as those developed for the earlier Smithsonian Widefield Infrared Camera on the MMT (Brown 2008). This controller is in turn derived from the CCD controller used for all of our instruments for the past few years. The system was developed to be simply extensible to as many as 72 readout channels running simultaneously at a 180 kHz pixel rate. Data acquisition and camera control is handled by a fiber-optically coupled commercial interface module from EDT, which mounts on the I/O board of the camera control unit. The critical task of taking the 32-channel video outputs from the preamplifier modules and converting to digital information is accomplished on custom A/D boards.

The HAWAII-2 imager plugs into a Yamaichi zero-insertion force (ZIF) socket, soldered to a 7 inch diameter cold header printed circuit board (PCB). This assembly serves the functions of routing signals to and from the imager, lateral and axial support for the spring-loading of the imager array against its precision locating structure, and as the main cooling mechanism for the imager and buffer amplifiers.

The signals to and from the cold HAWAII-2 array are carried on custom flexible printed circuits, terminating on four hermetic connectors soldered to four external preamplifier modules spaced around an aluminum mounting ring. This ring serves

as system ground for the camera system, and is electrically isolated from the rest of the structure and associated electrical grounds. The rest of the camera controller and associated power supplies reference to this ground.

All signals and power connections coming from and going to the camera controller are carried on RG-174 coax cabling to each of the four preamplifier modules. There is a 37-pin D-connector on the bottom of the backplane that supplies all required DC voltages and also the digital drive signals for the imager multiplexer. Each four-channel video section also has a dedicated 25-pin D-connector on the backplane.

In the laboratory we explored a wide range of detector settings and their impact on detector performance. VRESET, for example, affects both pixel well depth and dark current. Our final choice of operating voltages are BIASGATE $= 3.3$ V and VRESET $= 1$ V. The resulting detector performance (read noise, dark current, etc.) is discussed in § 10.

6. DESIGN ISSUES AND INNOVATIONS

6.1. Enhanced Slit Mask Wheel Cooling

The original design of MMIRS had the slit mask, Dekker, filter and grism wheels, and focus stage each cooled via sapphire ball bearings. Although formal calculations indicated that this would provide ample cooling, in practice this was not borne out. This shortcoming is believed to be because of the point contacts between the balls and the bearing grooves. Because the focus stage has a linear motion of only a few mm, adding copper straps was sufficient to solve the cooling problem there. The grism and filter wheels are enclosed in a box and do not require particularly fast cooldown and warmup, so radiative cooling is sufficient to cool them. The slit and Dekker wheels pose more of a challenge. They are required to cool to within 10 K of their final temperature within a ~ 5 hr period, and warm up similarly fast.

Our current design uses Energy Science Laboratory's Vel-Therm wrapped around the rotary shaft of the slit and Dekker wheels. Vel-Therm is a velvet material made of highly conductive carbon fibers that are epoxied into a backing material. We performed laboratory tests of Vel-Therm K40G-30B-M5 compressed to a thickness of 0.5 mm and found that its thermal conductivity was 630 W/ m-K at 300 K, 270 W /m-K at 135 K, and 170 W /m-K at 90 K.

The fibers of the Vel-Therm are canted downwards along the axis of the shaft, allowing them to bend but not buckle as the wheel changes direction. Teflon seals above and below the Vel-Therm trap any Vel-Therm fibers that may come loose from the backing material. With a Vel-Therm area of 18 cm^2, and a slit wheel mass of 6 kg, we measured in the lab a wheel cool-down time of 4 hr to cool within 20 K of the equilibrium temperature (85 K) and 6 hr to cool within 10 K. No temperature sensor is mounted on the wheel during regular operation. In normal operations we allot 5 hr for the wheel cool-down.

6.2. Gate Valve Seal Heaters

During preship testing we found that the gate valve once failed to seal properly when it was closed. The leak stopped during the instrument warmup, leading us to conclude that the gate valve blade had cooled by radiation, causing the Viton seal on the perimeter of the blade to harden. To solve this problem we epoxied a 6 W Kapton heater pad to the valve blade, along with a temperature sensor. When the instrument is cold we maintain the blade at -5°C and warm it up to 15°C when we exchange masks. Since the addition of the heater we have had no problems with gate valve leaks.

6.3. Gate Valve Thermal Glow and Enhanced Shielding

The gate valve separating the slit mask chamber from the main chamber makes it practical to change slit masks on a daily cycle but its seal must be near room temperature to seal properly. Because the warm gate valve is located between the cold slit mask and the cold collimator optics it must be carefully shielded to avoid intense thermal background through any filter that passes K-band light. We designed a cold spring-loaded baffle traveling on THK rails that passes through the open gate valve and nests into a fixed cold baffle above the first collimator lens. A cam on the gate valve blade raises the baffle above the gate valve as the valve is closed. Designing a smoothly operating baffle mechanism with sufficient travel to seal tightly took several iterations. For future infrared spectrograph designs we recommend using a cassette of cold slit masks that are admitted through a gate valve above the telescope focus. This arrangement eliminates all warm surfaces below the slit (e.g., Fabricant et al. 2012).

6.4. Warm-up Heater Adhesion Failure

The original warmup heaters for MMIRS were Minco foil heaters epoxied to the curved surfaces of the two LN_2 vessels with Lord 3170 epoxy. After the first warmup of the slit mask dewar from 77 K to room temperature, we found that eight of the 12 heaters were debonded from the vessel and melted. Rather than conduct an extensive investigation and requalification program for this type of heater, we switched to cartridge heaters soldered into copper blocks and bolted to the top surfaces of the two dewars. These heaters have performed without any problem.

6.5. Coating Failure

After ~ 2 yr of operation, we noticed that the antireflection coating on the inner surface of the second corrector lens had failed, becoming soft and iridescent with reduced throughput. This lens is cooled and warmed up whenever the slit masks are replaced, so we suspect a manufacturing issue exacerbated by thermal cycling. We manufactured and installed a replacement lens that is showing no degradation after 1 yr of operation.

6.6. Intermittent HAWAII-2 Electronics

The MMIRS detector is a first-generation 2048×2048 pixel HAWAII-2 detector and unfortunately one of its 32 output channels is now failing. When the output fails, 6% of the spectra are lost. The failure is intermittent, with an average failure rate of 10%, ranging on different nights between essentially zero frames up to 25–35%. This intermittent failure could be intrinsic to the array or could be associated with the readout electronics and cabling. The intermittent nature of the failure and the cryogenic environment make the problem difficult to diagnose.

In the years since we purchased the HAWAII-2, IR array technology and the associated readout electronics have progressed significantly. Current HAWAII-2RG arrays have greater reliability, higher and more uniform quantum efficiency, greater bias stability, better linearity, reduced image persistence, and an order of magnitude lower dark current than our installed array. Further, application-specific integrated circuits (ASICs) are available for the new arrays to provide simpler, high-reliability readout electronics with much simpler cabling. We have begun a ~1 yr-long effort to purchase and install a new HAWAII2-RG array in MMIRS, and hope to complete this process in the fall of 2013.

7. SOFTWARE

7.1. Overview

The MMIRS software supports slit mask design, instrument preparation procedures, night-time observing, and pipeline data reduction. The majority of MMIRS software is written in Tcl with some low-level code written in C. The system's client/server architecture is implemented using a simple ASCII over TCP sockets protocol. Typically, a server controls each hardware subsystem. Server commands expose the hardware functions to the user interface and to script clients that are used to operate the instrument. To minimize external dependencies, all interfaces with the Magellan or MMT facilities are localized in a single site-specific telescope server component. The MMIRS observing manual contains detailed instructions on running the slit mask design and observing software.

7.2. Slit Mask Design Software

MMIRS slit masks are laser cut into black-anodized aluminum blanks 75–200 μm thick. The observer downloads and runs the slit mask design program well in advance of a run to generate the mask files that are later converted into laser cutter commands. The observer uses a graphical user interface (GUI) to enter input parameters and the name of a catalog of observing targets. The catalog identifies targets with their priorities, mask alignment stars, and the minimum and maximum number of slits allocated for each target priority. A set of disperser/filter combinations is chosen and the mask design is valid for observation with the specified combinations. A field center or list of field centers for each proposed mask is provided and the software will attempt to optimize the number of slits fit by varying the mask position angle. If multiple masks are fit at the same time the distribution of targets on each mask will be optimized between masks. The user interface retrieves candidate wavefront sensor and guide stars from the GSC2 catalog and the availability of appropriate stars is verified for each mask position.

Following mask optimization, the user is presented with a list of mask designs ranked by the number of targets fit-weighted by user priority. Selecting a mask design from this list displays the mask overlaid on a FITS (Flexible Image Transport System) image of the field. The overlay marks targets, slits, guider and wavefront sensor regions, and candidate guide stars. A second display shows dispersed spectral regions superposed on a graphic of the detector array. Two text windows display the target catalog and the mask design with slits and targets. Selecting a line in either window highlights the corresponding target or slit in the graphical displays. After reviewing the possible mask designs the user selects the final mask files to be forwarded for fabrication.

7.3. Instrument Preparation Software

The MMIRS instrument specialists on the Magellan staff oversee thermal cycling of MMIRS through a dedicated user interface. The instrument specialist selects the desired operation: (1) initial cool down of the slit mask and camera sections at the start of a run, (2) slit mask exchange, or (3) warmup of both instrument sections at the end of a run. The instrument specialist executes each step of the procedure as directed by the program. The software checks that temperature, pressure, and motion stage positions are correct before proceeding. If a procedure is blocked, a text message directs the instrument specialist to address the listed issues.

7.4. Wavefront Sensor and Guide Star Acquisition Software

The telescope operator interacts with the wavefront sensor/guide star acquisition interface to choose appropriate stars for use in both guide cameras. The operator is presented with a star chart showing the stars of appropriate magnitude available in each of the guide camera patrol regions. Selecting a star moves the camera to that star and allows it to be centered in the wavefront sensor aperture or guide camera.

7.5. Slit Mask and Long Slit Alignment Software

After the telescope operator has acquired the guide stars, the observer must align the mask or long slit prior to observing. This procedure is carried out by following a sequence of steps presented to the observer in the mask alignment interface. The mask alignment software measures the relative offset between

the mask alignment stars and the centers of the alignment boxes cut in the mask using a pair of science detector images. If the field is not well enough aligned to allow the alignment stars to be viewed through their boxes, the images are taken with the slit mask removed, and the box positions are estimated from the nominal positions in the mask design file. A least squares fit of the position errors of the alignment stars is presented to the user and stars with large errors can be discarded. When a good fit is achieved, the computed position error is sent to the telescope as a guide correction. This process is iterated until the mask is properly aligned on the sky. The alignment software also creates a telescope offset catalog that is used to successively place a telluric calibration star in each of several slits. A similar procedure is followed to align long slits. Alignment of a slit mask typically takes 5–10 minutes.

7.6. Observing Interface

The observing interface allows the user to start MMIRS from a complete shutdown and to acquire science images in either manual mode or observing catalog mode. In manual mode, the observation is fully specified from the interface and the user presses "Go" to take a single exposure. In catalog mode, an input catalog specifies a subset of the observing parameters, e.g., filter, mask, exposure time, etc. Catalog-specified parameters are disabled on the interface. When "Go" is pressed, an exposure is taken for each row in the observing catalog. Prepared catalogs are available to automate calibration sequences and dark exposures. An instrument status window displays a schematic drawing of the MMIRS's current mechanical state, showing the positions of the motion stages and the current exposure status.

7.7. Data Archive

Three copies of the original data are made for archival purposes. After each exposure the data are copied to an observer directory for analysis and observer transport to their home institutions. Each day the LCO staff makes a second copy for the archive in La Serena. Finally, a third copy to an external hard drive is prepared for shipment to the CfA where the data are imported into a permanent online archive.

7.8. Engineering Software

Additional engineering software interfaces allow troubleshooting of the motion control and cryogenic/vacuum systems. Access to low-level motor control and status as well as individual temperature and pressure sensors are available from these interfaces. These interfaces are not intended for use during normal observing procedures.

7.9. Data Reduction Pipeline

7.9.1. Pipeline Overview

The MMIRS long-slit and multislit data reduction pipeline is a stand-alone package implemented in IDL with the first step implemented in C++. Complete details will be provided in a future paper (Chilingarian et al., in preparation); here we give an overview of the pipeline.

The pipeline is controlled by a task control file having a format similar to FITS headers, i.e., a set of keyword–value pairs where the keyword length is limited to eight characters and the total line length is limited to 80 characters. The control file can be created either in a text editor or by an automated system that analyzes observing logs. The control file can be edited in order to perform specific data reduction steps but by default the data are reduced completely until the sky subtraction step.

7.9.2. Primary Data Reduction and Wavelength Calibration

The primary data reduction includes the following steps:

1. Fitting the up-the-ramp slope in every pixel to produce a two-dimensional image for each exposure. This reduction is performed by the mmfixen package implemented in C++. mmfixen also corrects for detector nonlinearity and saturation. Hot pixels and pixels saturated in a single read are masked at this step.

2. Dark subtraction uses an average of up-the-ramp processed two-dimensional frames. We typically average five dark frames obtained for every readout interval and exposure time. We use different average dark frames for science exposures, flat fields, comparison spectra and telluric standards because different exposure times and readout intervals are used.

After the primary data reduction is complete, we subtract pairs of dithered spectral exposures (difference images hereafter) and bring them through the rest of the pipeline steps along with the individual exposures. We retain individual exposures to correctly propagate photon statistics to the final data products.

3. Scattered light subtraction is performed only for slit mask observations and is unnecessary for subtracted pairs of dithered spectra. The pipeline analyzes the mask definition files, then uses them to trace the spectra and gaps between spectra on a dark-subtracted flat field exposure. A model for scattered light is constructed from gap counts in all types of frames (science, flat, comparison spectra, telluric standards) using low-order polynomials along the dispersion direction and basic splines (*b*-splines hereafter) in the perpendicular direction. We cannot correct the ghost spectra arising from reflections from the mask back surface in this fashion. However, the amplitude of ghost images is about 1% of the flux in the corresponding slits and can be ignored unless very bright sources were observed or used as alignment stars. With long slits there are no gaps to allow modeling scattered light.

4. Mapping of optical distortions uses the spectral traces from the previous step. We use a low-order two-dimensional polynomial approximation to describe the distortion introduced by the optics and misalignment of the disperser relative to the detector array.

5. Extraction of two-dimensional spectra is performed only for slit mask data. The pipeline uses the mask definition files to extract two-dimensional spectra for each slit from the original frames without resampling. This operation is performed on both individual exposures and subtracted pairs.

6. Flat fielding is an important step in the data reduction as pixel-to-pixel variations in the detector reach 35%. Flat fielding also compensates for slit imperfections. We normalize the flux to unity using the 5×5 median-averaged frame as a reference to handle cosmic ray hits or hot pixel residuals. For slit mask data we normalize to the maximal flux within each slit to accommodate the intensity variations in the internal flat field calibrations.

7. Wavelength calibration differs for long-slit and slit mask data: the fit uses the entire frame for long-slit data and extracted two-dimensional frames for slit mask data. First, the Ar comparison lines are identified and an initial wavelength solution is fit with a two-dimensional third-order polynomial. Initial wavelength calibration of alignment stars uses an approximate one-dimensional dispersion relation because the calibration lines are blended due to the large alignment star apertures. The final wavelength solution uses OH airglow lines to refine the initial wavelength solution. A template spectrum for each aperture is extracted for a single pixel close to the frame center in the cross-dispersion direction. Spectra from adjacent pixels are cross-correlated with the template spectrum to measure and apply small residual wavelength shifts. This approach may fail when bright targets reduce the correlation coefficient between the template and adjacent pixels. In this case the same procedure can be performed on the comparison spectrum with a minor loss in accuracy.

7.9.3. Sky Subtraction

The subtraction of night sky emission is one of the most critical steps in the near infrared data reduction. The night sky emission includes bright OH emission lines and a continuum background that vary with time and pointing position. Faint targets observed with MMIRS can be hundreds of times fainter than the night sky level, so careful estimation of the sky background is essential.

In the MMIRS pipeline we use a hybrid approach to sky subtraction. The difference images that we create early in the pipeline are the first step in sky subtraction. However, the difference images contain residual night sky emission originating mostly from temporal variation of OH line flux. For a typical 300 s exposure these residuals may reach a few percent, so we apply a slightly modified version of the Kelson (2003) technique to the difference images. This technique uses spectra that have not been resampled and precise pixel-to-wavelength mapping to create an oversampled model of the night sky spectrum that is parameterized with b-splines and evaluated at every position at every slit. This techniques avoids artifacts from interpolation of undersampled night sky lines.

This Kelson approach works well on long-slit data where the slight shift in dispersion for off-axis rays allow good sampling of the emission line shape. For multiple-slit data, the short slit length doesn't allow full sampling. We used a modified approach creating the sky model from all of the slitlets assuming that their widths are equal. We must accommodate residual flat fielding errors along and perpendicular to the dispersion. We use a three-dimensional b-spline/polynomial parametrization where the b-splines are fit in the dispersion direction while two-dimensional Legendre polynomials that depend on X and Y slit positions account for the residual flat fielding errors. Our modified approach applied to the difference images leaves OH line residuals consistent with the Poisson photon statistics.

7.9.4. Final Cosmic Ray Rejection, Wavelength Calibration, and Rectification

After sky subtraction, we perform the final cosmic ray and hot pixel cleaning using the Laplacian filtering technique (van Dokkum 2001) on difference images. We modified the original code to handle negative and positive features because we are dealing with difference images. Wavelength calibration and geometric rectification are then applied using the distortion map and wavelength solutions derived in previous steps.

7.9.5. Telluric Correction

Telluric absorption correction is necessary to remove the variable OH absorption bands that punctuate near infrared spectra. We correct for this absorption by observing telluric standard stars, typically A0V stars with relatively featureless spectra observed at airmasses bracketing the science observations (Vacca et al. 2003). The observed spectra are compared with model predictions to derive a transmission curve. This procedure allows relative flux calibration of the data.

7.9.6. Final Data Products

The pipeline steps above produce calibrated two-dimensional difference images. A final two-dimensional spectrum is produced by inverting and adding the negative portion of the difference image. Finally, we extract one-dimensional spectra using optimal extraction with a double-Gaussian profile derived from alignment stars. The final data products are available in several formats: (1) multiextension FITS files with one extension for each two-dimensional co-added spectrum, (2) single-extension FITS files with all extracted one-dimensional spectra, (3) a Euro3D-FITS file (Kissler-Patig et al. 2004) for two-dimensional extracted spectra, and (4) a Euro3D-FITS file for one-dimensional extracted spectra. The first two files are accompanied by files in the same format providing flux uncertainties, while this

information is stored internally in the Euro3D-FITS format. MMIRS slit mask spectra in the Euro3D-FITS format contain metadata making them Virtual Observatory compliant (Chilingarian et al. 2006) and easy to visualize with the tools described in Chilingarian et al. (2008).

8. DAYTIME OPERATIONS

8.1. Slit Mask Exchange Procedure

The MMIRS slit mask wheel holds nine slit masks that are typically exchanged during day time by mountain staff. The procedure takes 10–11 hrs: 5 hr for warm up, 1 hr for mask exchange, and 4–5 hr for cool down. A step by step software procedure guides the mask exchange operator through the process. The interlock system is an additional safety mechanism to prevent damage to the optics and detector.

While the slit mask chamber is warming up, the slit mask operator uses a pull down menu to select the masks to be installed in each of the nine slots. When the process is complete, the mask configuration is saved and an observing catalog and mask exchange plan printout is created. After the slit masks are installed and cooled down to operating temperature, the masks are illuminated and a FITS reference file for each mask is recorded.

8.2. Controlled Cool-down

The cool-down and warmup of the optics section of MMIRS is controlled to minimize stress on the optics and detector. The cool-down control is accomplished with a Valcor cryogenic valve, an Omega temperature controller, and an RTD mounted on the curved back surface of the dewar at the end under the detector. The set point is ramped downwards at 0.15 K min^{-1} through software. A threshold prevents the set point from dropping more than 5 K below the actual temperature. This is a safety feature so that if the flow of cryogen is temporarily interrupted and then restored (e.g., when swapping from an empty LN_2 tank to a full one) there will not be a sudden drop in temperature. A 1.6 mm orifice at the end of the LN_2 fill line prevents the maximum flow rate of LN_2 from exceeding the nominal flow rate by more than a factor of 2, guarding against rapid cooling in the unlikely event that the valve sticks open.

The warmup is controlled in a similar manner. Cartridge heaters soldered into a copper block are bolted to the top of the optical bench. Additional low-power heaters are mounted onto the detector board. The detector board heaters, driven by a Lakeshore controller, are used to stabilize the temperature during normal operation. During warmup the detector board is ramped up at 0.15 K min^{-1} and the optical bench heater set point is set a few degrees below that of the detector board to minimize freezing outgassed material onto the detector. Again, thresholds prevent the set points from deviating from the actual temperatures so that loss of power will not cause a sudden drop in temperature.

Thermostats mounted on the heater blocks prevent current from going through the heater when the temperature rises above 40°C. The total heater power is limited to a level twice the nominal requirement. These features guard against catastrophic heating in the event of a control system failure.

9. OBSERVING PROTOCOLS

9.1. Introduction

For all observing modes, dark current is estimated from dark frames taken at the end of every night. A script scans all the observations carried out during the night and compiles a list of dark exposures available for data reduction.

9.2. Imaging

Imaging exposures normally use a pseudorandom dithering pattern within a specified square region larger than the target's extent, typically $30'' \times 30''$ to $180'' \times 180''$. Observing dithering catalogs including 100 pseudorandom positions are calculated by the observing software once the observer specifies the exposure time. Exposure times should not exceed 30 s in the K band, 60 s in the J and H bands, and 120 s in the Y band in order to avoid saturation by the sky background and bright field stars.

Twilight and internal flat field images should be acquired during the same night or at least during the same observing run. Normally, there is no need to take photometric standards as MMIRS's large field of view contains numerous 2MASS (Two Micron All Sky Survey) sources that supply absolute photometric calibration.

9.3. Long-Slit Spectroscopy

Following alignment we recommend dithering the target between three to five equally separated positions along the slit. The separation between dithering positions should normally exceed the target spatial extent and is typically 10–120″. Exposure times depend on the source and typically range from 5–10 s with 1 s readout intervals for bright stars to 600 s with 10 s readout intervals for faint targets. We recommend 300 s exposures with 5 s readout intervals for faint targets.

Long-slit observations require the following calibrations: (1) Ar comparison spectra and internal flat field frames at least once for each target and at 2 hr intervals for long integrations, and (2) multiple telluric standard stars (A0V spectral type) observed at the range of airmasses encountered.

9.4. Multiobject Spectroscopy

Following alignment we recommend dithering the target along the slit as described above. The optimal dithering spacings are a multiple of 0″.2 to shift by an integer number of pixels. Two position dithering is usually selected for bright targets, while four-position dithering can be used to improve sky subtraction. The standard slit height is 6–7″, so typical choices

TABLE 6
HAWAII-2 Operating Characteristics

Property	Typical performance
Gain	$5\ e^-$ DN^{-1}
Read noise (double correlated read)	$17\ e^-$
Read noise (60 reads)	$5\ e^-$
Full well	$230,000\ e^-$ or 46,000 DN
Linearity correction	usable to 41,000 DN (90% of full well)
Dark current	0.1 to 0.3 e^-s^{-1} pix^{-1} at 78 K
Readout time	32 channels at 180 kHz: 0.7 sec per read
Multiple sampling mode	"up-the-ramp"

are $\pm 2''$ or $\pm 1.8''$ and $\pm 1.4''$ where the reference is centered along the slits. The recommended exposure strategy is the same as that used for long slit observations.

We recommend the same sequence of calibration exposures as for long slits described above. The Ar comparison and internal flats should be obtained before moving the mask wheel because the repeatability of the wheel position is not perfect. A script aids in acquiring telluric standards by placing the standard star into every slit or at least into five representative slits: central, leftmost, rightmost, lowermost, and uppermost. The procedure covers the maximum wavelength range and assesses transmission variations across the field of view.

10. SCIENTIFIC PERFORMANCE

10.1. HAWAII-2 Array Performance

10.1.1. Readout Scheme and Readout Noise

Our standard readout mode for exposures longer than 30 s is "up-the-ramp", where we read out the detector non-destructively every 5 s. We perform a linear least squares fit to the series of readouts to determine the count rate for each pixel, rejecting anomalous intervals affected by cosmic ray hits. Up-ramp-mode also allows increased dynamic range because data from pixels which saturate part-way through the exposure can still be used. In a typical 300 s spectroscopic exposure the read noise is reduced from $17\ e^-$ for a double-correlated read to $5\ e^-$ for up-the-ramp sampling. Better performance could be obtained with a HAWAII-2RG array and by increasing the number of readouts. Table 6 summarizes the performance of our HAWAII-2 array with our current readout scheme.

10.1.2. Dark Current

The dark current in the detector currently dominates the noise performance for J- and H-band spectra. The current median dark current is 0.1 to $0.3\ e^-$ pixel^{-1} s^{-1} at 78 K, depending on the recent illumination of the detector. The dark current is higher in the corners of the device. The lowest dark current measured in the laboratory was $0.08\ e^-$ pixel^{-1} s^{-1} at 80.5 K, which after compensating for the temperature difference is a factor of 2 lower than the current value. The lower dark current was achieved with a VRESET $= 0.75$ V instead of the current 1.0 V. Lowering VRESET to 0.75 V reduces the full well capacity by 25%. The dark current increases after the detector is exposed to light; this effect is known as image persistence. For example, the dark current will be higher for many minutes after taking a mask alignment image. Replacing the HAWAII-2 detector with a HAWAII-2RG will decrease the dark current by an order of magnitude.

10.1.3. Linearity and Full-well Depth

The electronics gain is set at $5\ e^-$ DN^{-1}. Our choice of VRESET provides a pixel full well depth of $230,000\ e^-$, or 46,000 DN. Tests indicate that the array is linear at the 1% level until counts reach 90% of full well depth.

10.1.4. Reset Anomaly

A reset anomaly is commonly found in HAWAII-2 detectors, including ours. After clearing the detector, the first read has systematically higher counts than subsequent reads in an up-the-ramp dark exposure. The reset anomaly is repeatable, but we chose to minimize its effect by clearing the detector on a 5 s cadence between exposures.

TABLE 7
Imaging Characteristics

Property	Y	J	H	K
System throughput	0.25	0.22	0.29	0.26
Time to reach 50% saturation	600	400	50	65

TABLE 8
Imaging Vega Magnitude Limit for Signal/Noise of 10

Integration time in s	Y	J	H	K
60	20.3	20.1	19.5	18.8
300	21.2	21.0	20.4	19.7
3600	22.5	22.4	21.7	21.0

TABLE 9
SPECTROSCOPIC VEGA MAGNITUDE LIMIT FOR SIGNAL-TO-NOISE RATIO OF 10 PER RESOLUTION ELEMENT AT $R = 3$ 000 BETWEEN OH SKY LINES

Integration time in s	Y	J	H	K
3600	20.2	20.2	20.3	18.4

10.2. Backgrounds and Sensitivities

10.2.1. Interline background

The highest signal-to-noise ratio (S/N) regions of infrared spectra are found between the numerous OH airglow lines. After accounting for the known sources of internal backgrounds we can measure the intrinsic interline emission level. The best available estimate of the true interline background is the measurement by Maihara et al. (1993) of 590 photons $m^{-2}\,s^{-1}\,\mu m^{-1}$. We measure an H-band typical interline background that is 25% higher than the Maihara et al. (1993) value with no Moon illumination. Our measurement is consistent with recent measurements with very different spectrographs including Ellis (2012) through OH suppression fibers and Sullivan and Simcoe (2012) with a cross-dispersed echelle spectrograph. We refer the reader to the interesting discussions about the possible origin of this interline background in these two recent papers.

10.2.2. Thermal Emission from Gate Valve

Emission from warm surfaces in the gate valve provides an extra source of background in HK spectra. Improving the gate valve baffle has significantly reduced this background and has decreased the affected fraction of the detector. Tests performed with the K_s filter show that this background will be reduced below the level of the interline background with a new HK filter that cuts off at 2.35 μm, instead of the present 2.49 μm. The existing HK filter will remain available for those projects requiring coverage out to 2.49 μm.

10.2.3. Measured Throughput and Sensitivities

Table 7 gives the measured system throughputs and sky count rates for imaging. Throughput numbers were calculated by aperture photometry of a star in a 4″ diameter aperture and correcting for estimated extinction at 1 air mass. The throughput includes telescope reflectivity, transmission of the MMIRS optics and filters, as well as detector quantum efficiency. Introducing a disperser lowers throughput by ~30%. Measured imaging and spectroscopic sensitivities are given in Tables 8 and 9.

10.3. Sample Spectra

We conclude by displaying spectra of two faint galaxies that were acquired on the same aperture plate (Leiton et al., in preparation). These deep spectra of $H = 19.9$ and $H = 20.9$ galaxies displayed in Figures 10 and 11 demonstrate the performance of the instrument and pipeline reduction.

This material is based upon work supported by AURA through the National Science Foundation under Scientific Program Order No. 5 as issued for support of the Telescope Systems Instrumentation Program (TSIP), in accordance with Proposal No. AST-0335461 submitted by AURA.

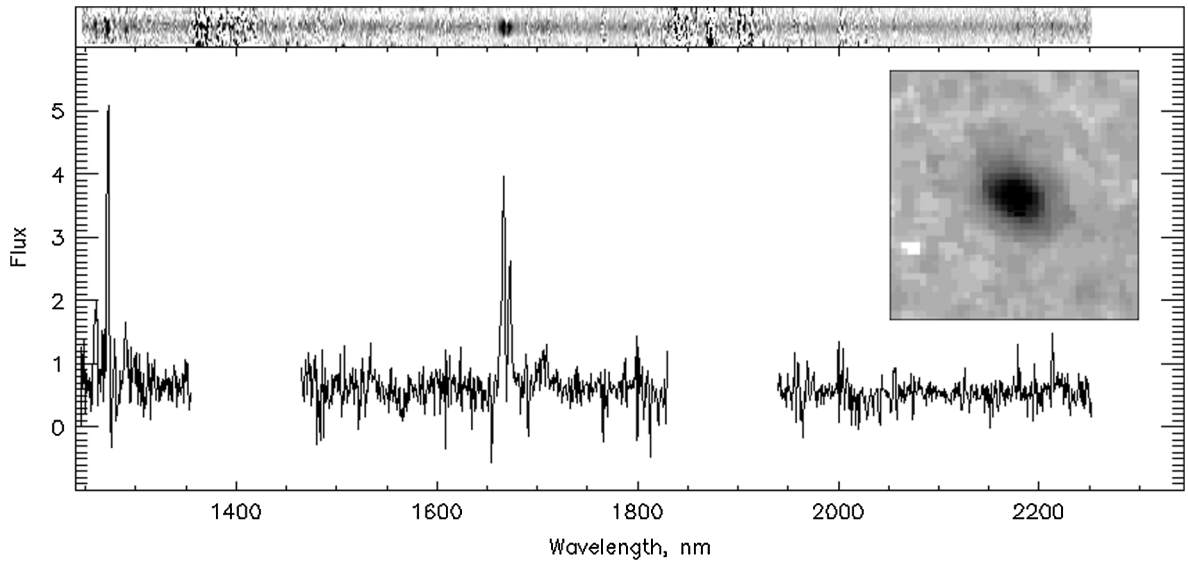

FIG. 10.—Spectrum of an $H = 19.9$ (Vega, $H_{AB} = 21.3$) Seyfert 2 galaxy at $z = 1.544$. [OIII] is visible at the blue end and Hα + [NII] is visible near the center of the spectrum. [SII] is the small bump at 1700 nm. The excellent OH sky line rejection of the MMIRS pipeline is apparent in this deep 7 hr exposure. The exposure time would be considerably reduced with a narrower slit (1″ slit used here), the higher-dispersion H grism, and the new HAWAII-2RG array. A Hubble Space Telescope image of the galaxy is shown in the inset; the scale is 2.5″ on a side. A two-dimensional image of the sky subtracted spectrum is visible at the top of the image.

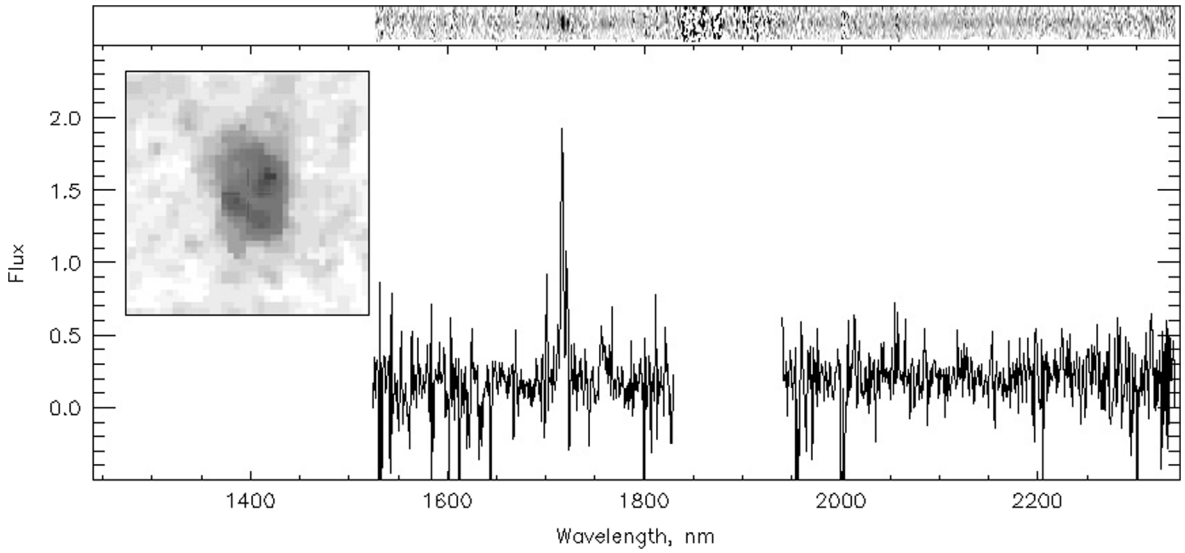

FIG. 11.—Spectrum of an $H = 20.9$ (Vega, $H_{AB} = 22.3$) star-forming galaxy at $z = 1.613$. As in the upper spectrum, Hα + [NII] is visible near the center of the spectrum, as well as a faint [SII] feature. The galaxies in Figures 10 and 11 were observed simultaneously; the different spectral coverage is due to the placement of the slit on the mask.

We thank the staffs of the MMT and Las Campanas Observatories for their tireless help during MMIRS commissioning. We thank Andrew Szentgyorgyi for his dedication and leadership commissioning the f/5 optics at Magellan. We thank S. Eikenberry, N. Raines, and J. Julian at the University of Florida for their support in making the FLAMINGOS 2 design available to the MMIRS design team.

REFERENCES

Barrera, S., et al. 2004, Proc. SPIE, 5495, 611
Bean, J. L., et al. 2011, ApJ, 743, 92
Brown, W. R. 2008, Proc. SPIE, 7014, 70142P
Brown, W. R., Epps, H. W., & Fabricant, D. G. 2004, PASP, 116, 833
Chilingarian, I., Bonnarel, F., Louys, M., & McDowell, J. 2006, in Astronomical Data Analysis Software and Systems XV, ed. C. Gabriel, C. Arviset, D. Ponz, & E. Solano (San Francisco: ASP) 351, 371
Chilingarian, I., Bonnarel, F., Louys, M., et al. 2008, in Astronomical Spectroscopy and Virtual Observatory (Noordwikj: ESAC) 125
Eikenberry, S., et al. 2006, Proc. SPIE, 6269, 626917
Elias, J., et al. 2006, Proc. SPIE, 6269, 62694C
Ellis, S. C., et al. 2012, MNRAS, 425, 1682
Elston, R. 1998, Proc. SPIE, 3354, 404
Elston, R., et al. 2003, Proc. SPIE, 4841, 1611
Epps, H., & Elston, R. 2003, Proc. SPIE, 4841, 1280
Epps, H., & Fabricant, D. 1997, AJ, 113, 439
Fabricant, D., et al. 2012, Proc. SPIE, 8446, 84461O
Garzon, F., et al. 2006, Proc. SPIE, 6269, 40
Hashimoto, T., Ouchi, M., Shimasaku, K., et al. 2012, in press (arXiv:1206.2316)
Hart, A., et al. 2011, BAAS, 43, 130
Kelson, D. D. 2003, PASP, 115, 688
Kewley, L., & Dopita, M.A. 2002, ApJS, 142, 35
Kewley, L., Geller, M., & Jansen, R. 2004, AJ, 127, 2002
Kissler-Patig, M., Copin, Y., Ferruit, P., Pécontal-Rousset, A., & Roth, M. M. 2004, Astronomische Nachrichten, 325, 159
McLean, I. S., et al. 2012, Proc. SPIE, 8446, 84460J (arXiv:1208.0314)
Leviton, D. B., Frey, B. J., & Kvamme, T. 2005, Proc. SPIE, 5904, 222
Leviton, D. B., Frey, B. J., & Madison, T. J. 2007, Proc. SPIE, 6692, 669204
Maihara, T., et al. 1993, PASP, 105, 940
McLeod, B., et al. 2004, Proc. SPIE, 5492, 1306
Otsuka, M., et al. 2011, ApJ, 729, 39
Pickering, T. E., West, S. C., & Fabricant, D. G. 2004, Proc. SPIE, 5489, 1041
Schechter, P. L., Burley, G. S., Hull, C. L., et al. 2003, Proc. SPIE, 4837, 619
Seifert, W., et al. 2010, Proc. SPIE, 7735, 292
Servillat, M., et al. 2011, AAS HEAD Division, 12, 13
Su, D., Zhou, B., & Yu, X. 1990, Sci China A, 33, 454
Sullivan, P., & Simcoe, R. 2012, PASP, in press (arXiv:1207.0817)
Suzuki, R., et al. 2008, PASJ, 60, 1347
Vacca, W. D., Cushing, M. C., & Rayner, J. T. 2003, PASP, 115, 389
van Dokkum, P. G. 2001, PASP, 113, 1420
Wilson, R. N. 1996, Reflecting Telescope Optics I (Berlin: Springer), 353